Journal of Molecular Liquids 385 (2023) 122394

Contents lists available at ScienceDirect

Journal of Molecular Liquids

journal homepage: www.elsevier.com/locate/molliq

# Separation of $CO_2/N_2$ mixtures by new IL/Acrylic polymer microcapsules designed by a one-step suspension-based polymerization encapsulation process

Rafael Duczinski [a,b], Barbara B. Polesso [a,b], Evandro Duarte [a,b], Franciele L. Bernard [a], Vitaly V. Chaban [c], Sandra Einloft [a,b,*]

[a] School of Technology - Pontifical Catholic University of Rio Grande do Sul – PUCRS, Av. Ipiranga, 6681, Building 30 – Room 101.08, Zip Code 90619-900, Porto Alegre, Brazil
[b] Post-Graduation Program in Materials Engineering and Technology – Pontifical Catholic University of Rio Grande do Sul – PUCRS, Brazil
[c] Yerevan State University, Yerevan 0025, Armenia

ARTICLE INFO

*Keywords:*
Microcapsules
Ionic liquids
$CO_2$ uptake
Selectivity

ABSTRACT

In this study, we developed a one-step simplified suspension-based polymerization process for encapsuling ionic liquids (ILs) ([emim][TfO] and [emim][$Tf_2N$]). Acrylic photoreactive monomers were cured using UV-365 light during the encapsulation process forming the capsule shell. The acetone extraction test confirmed IL encapsulation proving a high encapsulation efficiency for all samples (>80 %). For capsules produced with lower IL content, a homogeneous morphology was observed when compared to capsules with higher IL content. Suspension polymerization produced microcapsules presenting polynuclear morphology, as seen in TEM analysis. $CO_2$ sorption ability and $CO_2/N_2$ selectivity of the produced capsules were superior when compared to pristine shell material. Capsule stability was proved by submitting the samples to several sorption/desorption cycles. [emim][TfO] microcapsules with low ILs concentration presented superior $CO_2$ sorption results, 53 ± 0.9 $mgCO_2.g^{-1}$ (0.4 Mpa at 45 °C), and $CO_2/N_2$ selectivity, 4.5 ± 0.2, compared to [emim][$Tf_2N$] microcapsules. The improvement in sorption capacity of [emim][TfO] microcapsules was greater than 50 % in comparison with the pristine shell material. Electronic structure modeling corroborated the experimental results proving that [emim][TfO] is better to separate $CO_2/N_2$ thanks to three electron-rich oxygens. The sorption results allied to the easiness of the process represents a significant contribution to the scientific development of a new, efficient, and simplified method for the encapsulation of ionic liquids, which can be applied in the capture of $CO_2$ in industrial exhaust gas streams.

## 1. Introduction

In the 21st century, humankind is facing severe natural events such as rainfall volumes above historical averages, and extreme heat and cold waves [1,2]. These changes are being reported and discussed over the years by the scientific community. There is a consensus pointing to the burning of fossil fuels as the main source of carbon dioxide ($CO_2$) emissions, intensifying the greenhouse effect and heating the planet. [3,4]. Compared to the pre-industrial period, $CO_2$ concentration in the atmosphere is currently 47 % higher [5]. $CO_2$ emission from the burning of fossil fuels for energy generation handles about 60 % of the greenhouse effect [6]. EU member countries and China, for example, plan to achieve $CO_2$ neutrality by 2050 and 2060 respectively [7–9]. These targets aim to limit the increase in the earth's average temperature to 1.5–2 °C compared to the pre-industrial period [6,9]. To achieve these goals, using fossil fuels for energy generation, demands the creation of efficient and economically viable technologies for $CO_2$ capture and storage (CCS) or capture and utilization (CCU) [7,8,10].

CCS technologies are divided into pre-combustion, post-combustion, and oxy-combustion. Each technology presents specific characteristics of $CO_2$ content and pressure being the $CO_2$ separation process defined by these parameters [7,9,11]. $CO_2$ separation carried out using chemical absorption by amines aqueous solutions is the benchmark technology to date. Capture plants with amine solutions have high selectivity and their

* Corresponding author.
*E-mail address:* einloft@pucrs.br (S. Einloft).

https://doi.org/10.1016/j.molliq.2023.122394
Received 4 November 2022; Received in revised form 22 May 2023; Accepted 16 June 2023
Available online 17 June 2023

integration into industrial processes, compared to other technologies under development, is simpler [5]. The main aqueous amine solutions used in industry are monoethanolamine (MEA), diethanolamine (DEA), triethanolamine (TEA) and methyldiethanolamine (MDEA). [12,13]. However, chemical absorption by amines leads to major problems such as equipment corrosion, evaporation losses, and thermal and chemical degradation. The high energy penalty during the solvent regeneration step reduces capture plant efficiency [7,9].

$CO_2$ separation by physical adsorption using solid adsorbents appears as an alternative to amine-based chemical absorption presenting advantages such as adsorbent stability, easy regeneration, low or no equipment corrosion, and lower $CO_2$ regeneration energy consumption [5,9,14]. The $CO_2$ adsorption heat varies between 25 $kJ.mol^{-1}$ and 50 $kJ.mol^{-1}$ while for processes involving absorption by chemical solvents is about 185 $kJ.mol^{-1}$ [9,14]. Several kinds of solid adsorbents evaluated for $CO_2$ capture are described in the literature, such as zeolites, silica, MOFs, carbon-based materials, natural clays, alumina, and polymers. [13,15]. Porous solid adsorbents present high specific surface area and pore volume contributing to $CO_2$ capture. Nevertheless, some inconveniences such as low moisture tolerance, low $CO_2$ affinity, and loss of adsorption capacity at elevated temperatures are also described [13,16].

Ionic liquids (ILs) are an alternative for $CO_2$ capture processes. RTILs are liquid solvents below 100 °C and formed by an organic cation and an organic or inorganic anion [12,17]. ILs have drawn great attention in recent years for application in $CO_2$ capture due to their unique properties such as high affinity for the $CO_2$ molecule, thermal stability, low vapor pressure, low flammability, and selectivity for $CO_2$ in the presence of gases such as $N_2$ and $CH_4$ [7,17,18]. The use of ILs for $CO_2$ capture in industrial plants needs to overcome problems related to their high viscosity making their handling difficult, besides the high cost and the slow $CO_2$ adsorption/desorption kinetics [7,17]. Literature describes a portfolio of options to use ILs in large-scale processes for $CO_2$ capture, including the production of polymer micro and nanocapsules containing ILs [19,20]. Yet, physical and chemical immobilization of IL in solid supports, such as silica, activated carbon, zeolites, alumina, and MOFs [21–23], poly(ionic liquid) synthesis [24,25], IL encapsulation in silica [19], carbon [20] and polymers [12,26], are some examples of technologies under development to enable ILs industrial applications. The use of encapsulated ILs for application in $CO_2$ capture is still scarce in the literature. However, several techniques have been described for capsule production for different industrial applications. The main technics are microfluids, suspension polymerization, phase inversion, and interfacial polymerization [27–30]. The use of microcapsules to capture gases, such as $CO_2$, increases the contact area between the sorbent and the $CO_2$ appearing as a good option to further improve the process [31].

A simplified procedure for the ILs encapsulation, based on the suspension polymerization technique, was described in this work. Yet, the influence of different fluorinated anions on the encapsulation process was evaluated. The ILs [emim][TfO] and [emim][$Tf_2N$] were encapsulated at theoretical concentrations of 15 %, 30 % and 40 %. The microcapsules shell material was synthesized during encapsulation using a photoreactive acrylic polymer under ultraviolet light. The microcapsules production process using the methodology proposed in this work occurs in only one step. The encapsulation efficiency was evaluated as a function of the anion type and the amount of encapsulated IL. $CO_2$ sorption capacity and $CO_2/N_2$ selectivity for the produced capsules were evaluated as well.

## 2. Materials and methods

### 2.1. Reagents

1-methylimidazole (≥99 % Sigma Aldrich), 1-bromoethane (98 % Sigma Aldrich), bis(trifluoromethylsulfonyl)imide lithium salt (99,5 % Sigma Aldrich), acetonitrile (Sigma Aldrich), pentane (98 % Sigma Aldrich), 3-[Tris(trimethylsiloxy)]propyl methacrylate (*SiTRIS*, 98 % Sigma Aldrich), trimethylolpropane trimethacrylate (*TMPTMA*, Sigma Aldrich), 2-hydroxy-2-methylpropiophenone (D-1173, 97 % Sigma Aldrich), 1-ethyl-3-methylimidazolium trifluoromethanesulfonate ([emim][TfO], MM = 260.23 $g.mol^{-1}$) (≥98 % Sigma Aldrich), paraffin oil (Sigma Aldrich) and acetone.

### 2.2. [emim][$Tf_2N$] synthesis:

1-ethyl-3-methylimidazolium bis(trifluoromethylsulfonyl)imide ([emim][$Tf_2N$], MM = 391.31 $g.mol^{-1}$) RTIL was synthesized following procedures adapted from literature[32–34]. Firstly, 1-methylimidazole was dissolved in acetonitrile using a three-necked flask, then an excess of 1-bromoethane was added (molar ratio 1:1.5, respectively). The mixture was stirred under reflux for 24 h under $N_2$ atmosphere. The 1-ethyl-3-methylimidazolium bromide ([emim][Br]) was filtered, and volatile material was removed under vacuum (~$10^{-3}$ mbar). [emim][Br] and bis(trifluoromethylsulfonyl)imide lithium salt were added in a three-necked flask and dissolved using distilled water. The mixture was kept stirring for over 24 h in room temperature. The two phases were separated in a separatory funnel. The lower phase, containing the [emim][$Tf_2N$], was washed with distilled water several times and dried under vacuum. The structure of the RTILs was confirmed by Nuclear Magnetic Resonance, [emim][Br]: $H^1$ NMR (400 MHz, $CDCl_3$) δ ppm: 1.57 (t, 3H), 4.11 (s, 3H), 4.42 (q, 2H), 7.56 (s, 2H), 10.2 (s, 1H). [emim][$Tf_2N$] δ ppm: 1.48 (t, 3H), 3.96 (s, 3H), 4.16 (m, 2H), 7.19 (s, 1H), 7.35 (s, 1H) and 8.52 (s, 1H).

### 2.3. Microcapsules synthesis:

The microcapsules were produced by the suspension synthesis method. Initially, the ideal ratio between SiTRIS, TMPTMA, and the photoinitiator D-1173 was determined to prepare a photoreactive solution. This solution, in the presence of ultraviolet light (UV-365, λ: 365 nm) produces the shell microcapsules. In an Eppendorf tube were added 0.69 mmol, 4.37 mmol, and 2.11 mmol of SiTRIS, TMPTMA, and D-1173, respectively. The solution was stirred in a vortex mixer (2000 RPM) for 2 min and then kept away from light. A small sample of the solution was exposed to UV-365 light to confirm its photoreactivity, as seen in Fig. 1. The encapsulation process shown in Fig. 2 was carried out by adding the ILs theoretical mass, the photoreactive solution, and the paraffin oil to a test tube. The tube is vortexed for 5 min until the capsules obtainment in the paraffin oil suspension. Then, the capsules are exposed to UV-365 light for a period of 5 to 7 min until the capsule shell is fully cured. The formed capsules are washed in pentane to remove the

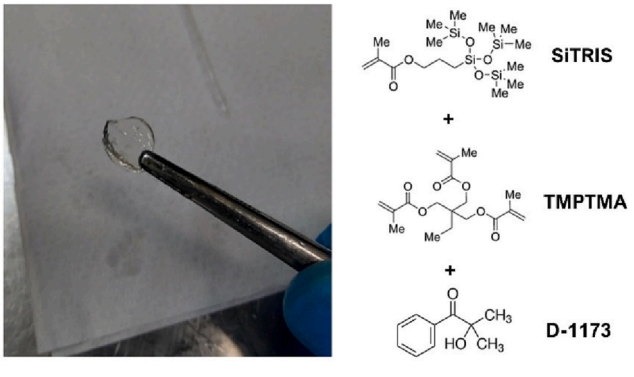


**Fig. 1.** Photoreactive solution of acrylic monomers SiTRIS (3-[Tris(trimethylsiloxy)]propyl methacrylate), TMPTMA (trimethylolpropane trimethacrylate) and the photoinitiator D-1173 (2-hydroxy-2-methylpropiophenone) after UV-365 exposition.

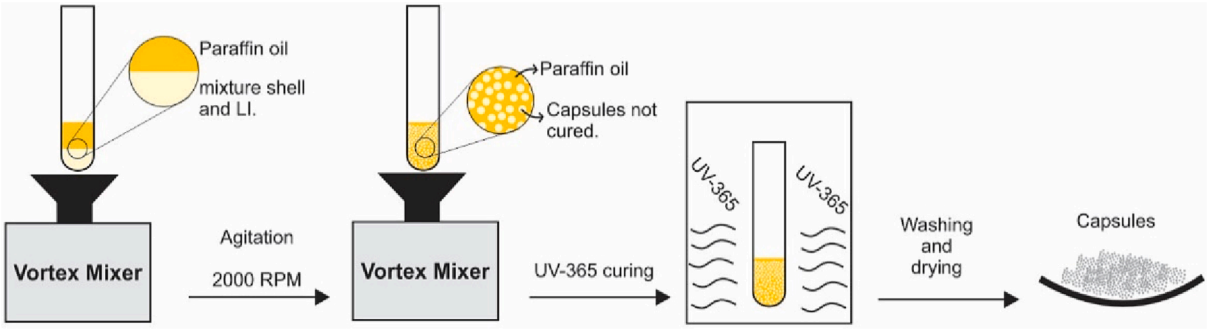


**Fig. 2.** Synthesis process used to capsule production: initially a microcapsule suspension has been formed by vortex agitation followed by UV-light exposure to finish the cure step. Formed microcapsules were washed and dried.

paraffin oil and then dried in an oven at 45 °C. Capsules with theoretical concentrations of 15 %, 30 % and 40 % were synthesized using the RTILs [emim][TfO] and [emim][$Tf_2N$], Fig. 3.

### 2.4. Microcapsules characterization:

The Bruker Avance DRX-400 spectrometer operating at 400 MHz was used to record the $^1H$ Nuclear Magnetic Resonance (NMR) spectra. FTIR spectra were recorded on a Parkin-Elmer Spectrum 100 spectrometer in universal attenuated total reflectance (UATR) mode. Energy dispersion mapping X-ray spectrometry (EDS), Field emission scanning electron microscopy (FESEM) were performed using FEI Inspect F50 equipment in secondary electrons mode. Particle size data were determined using ImageJ software. Transmission electron microscopy (TEM) was carried out using a Tecnai G2 T20 FEI operating at 200 kV. The ImageJ software was used in capsule size measurement. Thermal properties of microcapsules were assessed by differential scanning calorimetry (DSC) using a TA Instrument Q20 in the range from −90 °C to 40 °C at a heating rate of 10 °C.$min^{-1}$ under $N_2$ atmosphere. The acetone extraction method was used to determine the microcapsules' core content following literature procedures [12,35]. The mass of the accurately weighed dry microcapsules was recorded, and then the microcapsules were fully soaked in acetone for 72 h being the acetone solvent replaced every 24 h. Then, after the shell was dried and weighed. The % of encapsulated IL was calculated following equation (1).

$$\%IL_{encapsulated} = \frac{w_1 - w_2}{w_1} \times 100 \quad (1)$$

Where, $w_1$ = dry microcapsules mass weighed;
$w_2$ = dry microcapsules mass after extraction in acetone.

### 2.5. $CO_2$ experiments

$CO_2$ sorption capacity, sorption/desorption and selectivity ($CO_2/N_2$) tests were performed following the procedures previously described for our group [12,17,25,36] based on the pressure-decay technique using dual-chamber gas sorption, shown in Fig. 4.

#### 2.5.1. $CO_2$ sorption measurements

The experiments were carried out in triplicate in a gas sorption cell (Fig. 3) with previously degassed (70 °C for 2 h) samples (Ws ≈ 1 g). $CO_2$ sorption measurements were carried out at 45 °C and 0.4 MPa. The $CO_2$ sorption capacity ($W_{CO2/g}$) was calculated by equations (2) and (3).

$$n_{CO_2} = \frac{p_i V_{gc}}{Z_{(P_i,T_i)} R T_i} - \frac{p_{eq}(V_t - V_s)}{Z_{(P_{eq},T_{eq})} R T_{eq}}, \quad (2)$$

$$w_{CO_2.g^{-1}} = \frac{n_{CO_2} M}{w_s}, \quad (3)$$

Where n is the number of mols, $p_i$ and $T_i$ are the pressure and temperature in the gas chamber, $V_{gc}$ is the volume of the gas chamber, $p_{eq}$ and $T_{eq}$ are the pressure and temperature at equilibrium in the sorption chamber, $V_s$ is the volume of the sample, $V_t$ is the total volume of the sorption chamber, Z is compressibility factor for the pure gas calculated by Span-Wagner equations-of-state for $CO_2$ [37].

#### 2.5.2. Sorption and desorption tests

Five $CO_2$ sorption/desorption cycles were performed in ILs microcapsule samples. $CO_2$ sorption was evaluated at 45 °C and 0.4 MPa with desorption following each cycle using heating 70 °C for 2 h.

#### 2.5.3. $CO_2/N_2$ selectivity

The selectivity tests were carried out at 45 °C and 2 MPa with previously degassed samples ($W_s$ ≈ 1 g; 70 °C; 2 h) using a binary mixture (15.89 mol % of $CO_2$ and $N_2$ balance). $CO_2$ selectivity over $N_2$ was calculated following Equation (4)

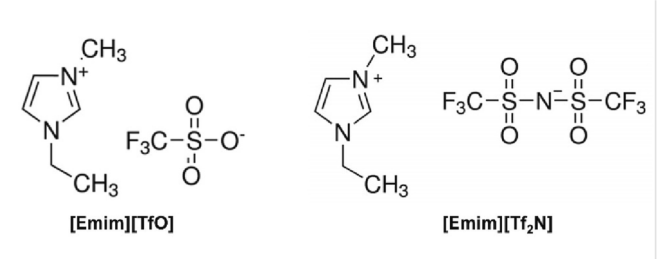


**Fig. 3.** Structure of [emim][TfO] (1-ethyl-3-methylimidazolium trifluoromethanesulfonate) and [emim][$Tf_2N$] (1-ethyl-3-methylimidazolium bis (trifluoromethylsulfonyl)imide) used in this work.

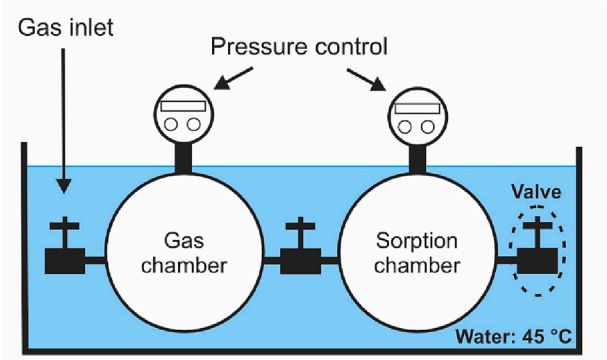


**Fig. 4.** Steel cell immersed in a water bath used to measure $CO_2$ sorption and $CO_2/N_2$ selectivity at temperature of 45 °C and equilibrium pressure of 0.4 MPa and 2 MPa, respectively.

$$S = \frac{X_{CO_2}/Y_{CO_2}}{X_{N_2}/Y_{N_2}}, \quad (4)$$

Where $X_{CO2}$ and $X_{N2}$ are molar fractions of $CO_2$ and $N_2$ in the sample phase and $Y_{CO2}$ and $Y_{N2}$ are molar fractions of $CO_2$ and $N_2$ in the gas phase, respectively.

#### 2.5.4. Eletronic-structure modeling

The electronic structures of the simulated systems were solved using the M11 hybrid density functional theory (DFT) [38]. The M11 model represents an approximation to the exchange–correlation energy functional that combines a certain portion of exact exchange from a Hartree-Fock calculation and a certain portion of the exchange–correlation energy from other sources. The chosen functional incorporates an attractive fraction of the van der Waals interactions. It is, therefore, suitable to accurately investigate non-covalent binding in systems that comprise several molecules of various polarities.

The atom-centered split-valence double-zeta polarized basis set was used to represent hydrogen, carbon, nitrogen, oxygen, fluorine, and sulfur atoms. The wave function was optimized iteratively according to the self-consistent field until the energy convergence criterion, $10^{-8}$ Hartree was attained. The geometries of the systems were optimized by minimizing all components of forces acting on atoms according to the rational function optimization algorithm. The following geometry convergence criteria were employed: 120 kJ $nm^{-1}$ for maximum force, 80 kJ $nm^{-1}$ for root-mean-squared force, 1.8-$10^{-3}$ nm for maximum displacement, and 1.2-$10^{-3}$ nm root-mean-squared displacement.

The reported binding energies were corrected for basis set superposition error through the counterpoise methodology. A few lowest-energy stationary points of each system were used to obtain and compare binding energies for various ion-molecular configurations. The analysis of vibrational frequencies was used to ensure that the chosen stationary points do not represent transition states. The partial electrostatic charges localized on every atom were computed according to the Merz-Singh-Kollman methodology.

The comprehensive scans of the potential energy surfaces of the simulated systems were performed according to the following methodology [39,40]. One hundred immediate molecular configurations were obtained from PM7–MD simulations [41–44] at 400 K. Each of these configurations was optimized to remove an effect of thermal energy. The optimized geometries were arranged according to their potential energies. The lowest-energy configuration of each system was considered to be its global minimum. Several essentially different local minimum structures were used as initial guesses in hybrid DFT calculations as described above.

Each electronic-structure calculation used eight processor cores. GAMESS 2020 was used to conduct DFT calculations [45]. MOPAC 2016 (https://openmopac.net) was used to conduct semiempirical calculations. PM7-MD 1.7 was used to simulate dynamics at a finite temperature [46]. GMSEARCH 2.0 was used to scan potential energy surfaces. Gabedit 2.5 was used to prepare initial Z-matrices and visualize ultimate ion-molecular geometries [47].

## 3. Results and discussion

Suspension polymerization allows the synthesis of microcapsules with uniform shell diameter and thickness [28]. Yet, the combination of different ILs in the core and polymers to form the shell can be explored resulting in capsules with different properties [48,49]. Acrylic polymers are permeable to gases such as $O_2$ and $CO_2$ besides an adjustable structure producing hardness and hydrophobicity to the microcapsules [48]. ILs [emim][TfO] and [emim][Tf2N] are known to have affinity for $CO_2$ molecules, besides being miscible in the curing solution containing the monomers for the microcapsules shell formation [50]. The synthesis method via suspension polymerization used in this work was performed in a one-step simplified way evaluating the potential of this technique to be used to produce capsules for $CO_2$ capture processes.

### 3.1. Acetone test

The ILs [emim][$Tf_2N$] and [emim][TfO] were encapsulated with theoretical values of 15, 30 and 40 % of IL regarding the microcapsule weight. The acetone extraction test was used to determine the encapsulation efficiency concerning the theoretical amount. Table 1 shows the results for each sample. The IL encapsulation was inferior when compared to the theoretical concentration. However, the encapsulation efficiency for all samples remained above 80 %. The IL [emim][TfO] encapsulation efficiency [emim][TfO] was above 85 % for all samples at different IL concentrations.

### 3.2. FTIR analysis

Fig. 5 presents the FTIR spectra of the ILs [emim][$Tf_2N$] and [emim][TfO], the pristine shell and the IL encapsulated samples. For the IL [emim][$Tf_2N$] the bands at 3200–2800 $cm^{-1}$ are attributed to the C—H stretching vibration, at 1574 $cm^{-1}$ C—N symmetric and asymmetric stretching of imidazolium ring, and the band at 1347 $cm^{-1}$ and 1171–1050 $cm^{-1}$ to O═S═O asymmetric and symmetric stretching. The band at 788–739 $cm^{-1}$ is attributed to the group S—N—S, characteristic of the [$Tf_2N^-$] anion [51,52]. For the IL [emim][TfO], the band at 3200–3000 $cm^{-1}$ is attributed to the C—H stretching vibration, at 1636 $cm^{-1}$ the characteristic band of [$CF_3SO_3^-$], at 1574 $cm^{-1}$ C—N symmetric and asymmetric stretching of imidazolium ring, at 1250–1150 $cm^{-1}$ O═S═O symmetric stretching, at 1026 $cm^{-1}$ $SO_3$ symmetric stretching, and 756 $cm^{-1}$ $CF_3$ symmetric deformation [51–53]. For the pristine acrylic shell, the band at 3496 $cm^{-1}$ is attributed to C═O overtone stretching mode, at 2965 $cm^{-1}$ to $CH_3$—O symmetric stretching from the ester group, at 1726 $cm^{-1}$ an intense band attributed to C═O, at 1464 $cm^{-1}$ and 1412 $cm^{-1}$ asymmetric bending $CH_3$ and bending $CH_2$ vibration modes, respectively, at 1253 $cm^{-1}$ asymmetric stretching vibration C—O—C coupled with $CH_3$—O vibration modes [36,54,55]. The microcapsules with a theoretical concentration of 15 % (m/m) of the ILs are shown in Fig. 5 as an example confirming the ILs presence in the microcapsules. The spectra of the samples M15-$Tf_2N$ and M15-TfO present bands in regions characteristic of the ILs and the shell acrylic polymer, indicating the presence of ILs in the produced microcapsules.

### 3.3. DSC analyses

The ILs used in the encapsulation process and a pristine sample of the shell material were evaluated by DSC (see Fig. 6 and Table 2). The IL [emim][$Tf_2N$] undergoes an endothermic melting event between −31 °C

**Table 1**
Data of the produced microcapsules with ionic liquid types, theoretical encapsulation value predicted, true encapsulated ionic liquid percent and process efficiency.

| Sample | Ionic liquid (IL) | Theoretical value for IL encapsulation (%) | IL true encapsulated (%) | Encapsulation efficiency (%) |
|---|---|---|---|---|
| M15-$Tf_2N$ | [emim][$Tf_2N$] | 15 | 12.3 ± 0.3 | 82.0 |
| M30-$Tf_2N$ | | 30 | 25.2 ± 0.5 | 84.0 |
| M40-$Tf_2N$ | | 40 | 33.6 ± 0.4 | 83.5 |
| M15-TfO | [emim][TfO] | 15 | 13.0 ± 0.6 | 86.7 |
| M30-TfO | | 30 | 26.5 ± 0.2 | 88.3 |
| M40-TfO | | 40 | 35.7 ± 0.5 | 89.2 |

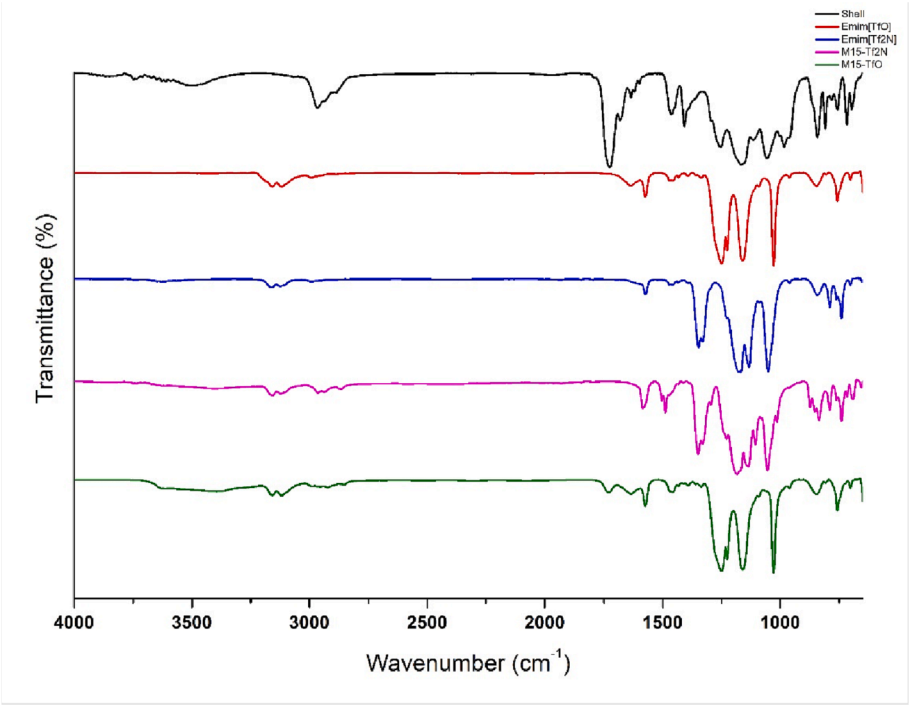


**Fig. 5.** Infrared spectrum data of ionic líquids [emim][$Tf_2N$] and [emim][TfO], pristine shell, and M15-$Tf_2N$ and M15-TfO microcapsules samples.

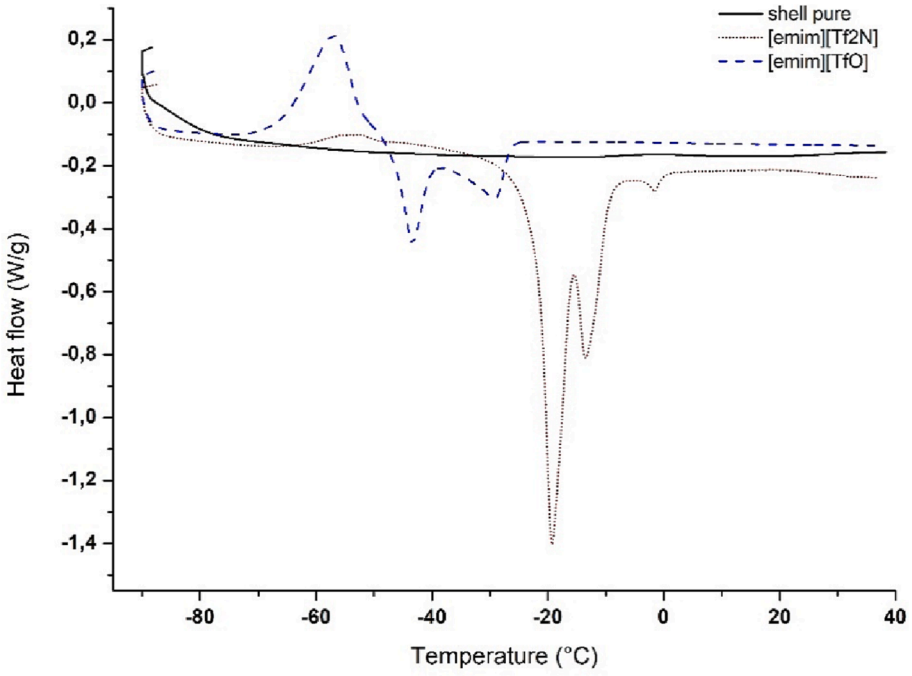


**Fig. 6.** Differential scanning calorimetry of neat ionic liquids [emim][$Tf_2N$] and [emim][TfO] and acrylic shell material used for microencapsulation process. The melting and crystallization events could be verified for all samples, except in the shell pure sample that do not present crystallization event.

and 4 °C. The IL [emim][TfO] undergoes an exothermic crystallization event between −73 °C and −48 °C, followed by a melting event in the temperature range between −75 °C and −23 °C. The difference in melting temperatures between the evaluated ILs is linked to the strength of the interaction between the cation and anion of each IL. This difference can also be observed in the ILs fusion enthalpies, indicating a stronger cohesive force between the ions of the ILs. For instance, IL [emim][$Tf_2N$] has a higher enthalpy of fusion ($\Delta H_m$ = 48.7 J.$g^{-1}$) than IL [emim][TfO] ($\Delta H_m$ = 38.0 J.$g^{-1}$) as shown in Table 2 [56,57]. Neither of the ILs displays glass transition. The pristine microcapsules shell polymer exhibits a slight melting event ranging −38 °C and −0.7 °C ($\Delta H_m$ = 2.8 J.$g^{-1}$) without any observed crystallization event. The structure of the microcapsules containing ILs was also evaluated (Fig. 7). Microcapsules containing the IL [emim][$Tf_2N$] (Fig. 7) exhibit low-intensity melting thermal events ($\Delta H_m$ < 1.0 J.$g^{-1}$, Table 2) at temperatures lower than those of the pure IL [emim][$Tf_2N$] and the shell. Microcapsules containing the IL [emim][TfO] (Fig. 7) in the capsule core show melting peaks at temperatures of −37 °C, −24 °C and −27 °C for

**Table 2**
Thermal Properties of the materials performed by differential scanning calorimetry (DSC) in the heating step analysis.

| Sample | Ionic liquid (IL) | $T_m$ (°C) | $T_c$ (°C) | $\Delta H_m$ (J. $g^{-1}$) | $\Delta H_c$ (J. $g^{-1}$) |
|---|---|---|---|---|---|
| Shell | | − 16 | | 2.8 | |
| [emim][$Tf_2N$] | | − 19; −13 and −1 | | 48.7 | |
| [emim][TfO] | | − 43 and −28 | − 57.0 | 38.0 | 35.0 |
| M15-$Tf_2N$ | [emim][$Tf_2N$] | − 29 | | 0.44 | |
| M30-$Tf_2N$ | | − 29 | | 0.41 | |
| M40-$Tf_2N$ | | −27 | | 0.28 | |
| M15-TfO | [emim][TfO] | − 37 | | 7.3 | |
| M30-TfO | | − 24 | | 3.1 | |
| M40-TfO | | − 27 | | 3.7 | |

samples with a theoretical percentage of 15 %, 30 %, and 40 %, respectively. The shifts of melting peaks vary with increasing IL concentration in the microcapsules, suggesting a correlation between concentration, melting temperature, and stronger interaction between the IL and the polymeric matrix of the shell [56,57]. For the M15-TfO, M30-TfO, and M40-TfO microcapsules, no thermal crystallization events were identified during the analysis.

### 3.4. TEM analysis

Capsules morphology (ILs M15-TfO and M15-Tf2N) are seen in Fig. 8. The M15-TfO microcapsule (Fig. 8A) has lighter areas spread throughout its structure. M15-Tf2N (Fig. 8B) has more evident nuclei with different sizes inside the same microcapsule. The morphology showed by the samples suggests that the encapsulation process is producing microcapsules with polynuclear morphology, corroborating literature findings [58]. Ekanem and collaborators obtained dual-core microcapsules by varying the injection volumetric flow rate of solutions of the internal, intermediate, and continuous phases using a glass capillary device [59]. Polynuclear microcapsules with up to four nuclei can be obtained by varying the flow in a microfluidic device [60]. The presence of the various nuclei difficult microcapsule wall thickness evaluation. The nuclei size is similar (see Fig. 8), indicating a good dispersion of the IL within the microcapsules.

### 3.5. $CO_2$ sorption and $CO_2/N_2$ selectivity analysis

$CO_2$ easily permeates acrylic polymers. This feature plays a crucial role in enabling the permeation of $CO_2$ through the capsule shell and into the IL located within the capsule core. This process is essential in facilitating efficient adsorption. The desorption step is also facilitated by the shell permeation capacity [48]. The $CO_2$ sorption capacity of microcapsules was evaluated and depicted in Fig. 9. The sorption capacity of the pristine acrylic polymer used as the shell was also evaluated presenting a $CO_2$ sorption capacity at 45 °C of 34 ± 1.2 $mgCO_2.g^{-1}$ (Fig. 9). The IL [emim][$Tf_2N$] concentration shows no influence in $CO_2$ sorption capacity for samples M15-Tf2N and M30-Tf2N (compare 45 ± 0.8 $mgCO_2.g^{-1}$ and 44.8 ± 1.2 $mgCO_2.g^{-1}$, respectively). However, at higher concentrations, there is a slight increase in the sorption capacity (49.2 ± 1.1 $mgCO_2.g^{-1}$ for sample M40-Tf2N). Comparing this value with the sorption capacity of the pristine shell material, an increase in sorption capacity of 44.7 % is observed. For the IL [emim][TfO] an opposite behavior was observed. M15-TfO presented a higher $CO_2$ sorption capacity (compare 53 ± 0.9 $mgCO_2.g^{-1}$ with 41.4 ± 1.4 $mgCO_2.g^{-1}$ (M30-TfO) and 47.3 ± 1.3 $mgCO_2.g^{-1}$ (M40-TfO)). The sorption capacity for M15-TfO is about 56 % higher compared to pristine shell material. The ILs concentration and morphology of microcapsules possibly influenced the obtained results. According to existing literature, the $CO_2$ solubility of [emim][TfO] is reported to be slightly lower than that of [emim][$Tf_2N$]. Moreover, it has been suggested that the unique morphology of [mim][TfO] microcapsules may have played a role in

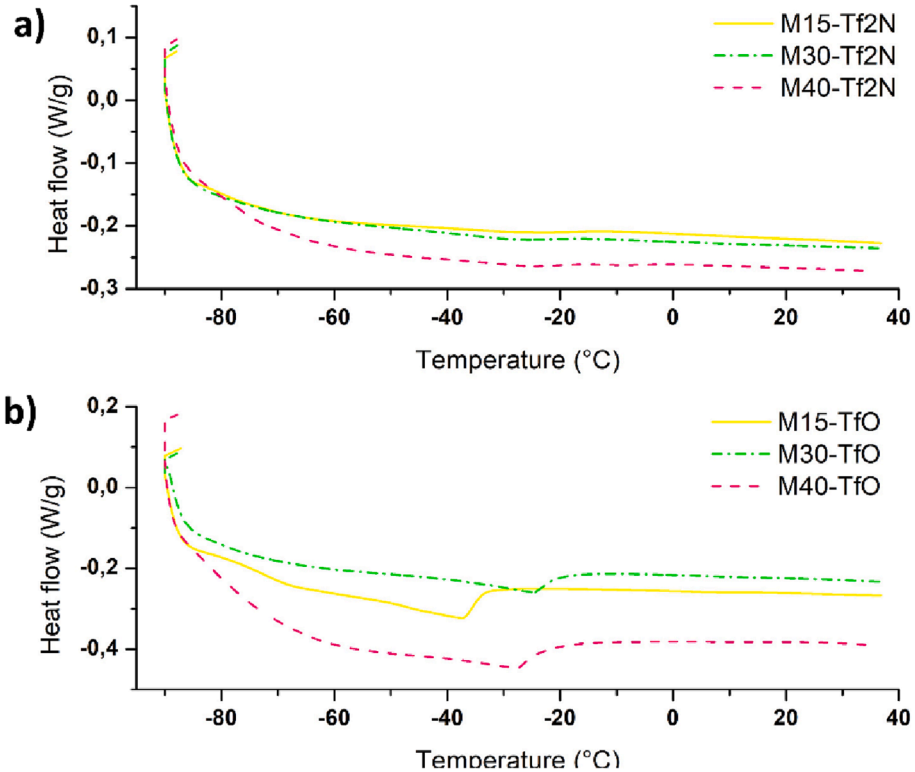


**Fig. 7.** Differential scanning calorimetry data for microcapsules samples containing different [emim][$Tf_2N$] (a) and [emim][TfO] (b) theorical concentrations (15 %, 30 % and 40 %).

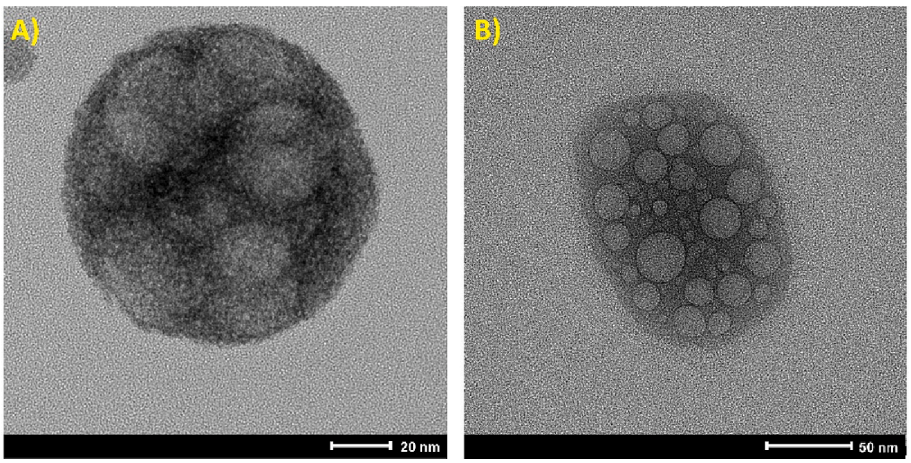


**Fig. 8.** Typical microcapsule morphology: A) M15-TfO and B) M15-$Tf_2N$.

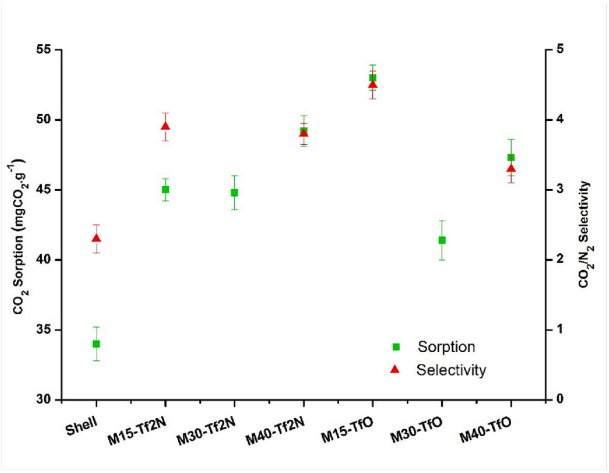


**Fig. 9.** $CO_2$ sorption capacity measured (0.4 Mpa, 45 °C) for the microcapsules synthesized with the ionic liquids [emim][$Tf_2N$] and [emim][TfO] with differents theorical ionic liquids concentrations (15 %, 30 % and 40 % (m/m)); The $CO_2/N_2$ selectivity of the samples with the lowest and heist amount of ionic liquids were also evaluated (2 Mpa, 45 °C).

improving the sorption results. The sorption capacity of M15-TfO is higher when compared to microcapsules reported in the literature [61,62]. [bmim][$Tf_2N$] polysulfone microcapsules containing metal oxide ($Fe_2O_3$) have been obtained and the $CO_2$ sorption capacity is below 50 $mgCO_2.g^{-1}$ at 0.4 MPa and 45 °C [62]. The amino acid-based ILs [bmim][GLY], [bmim][PRO] and [bmim][MET] after encapsulation in hollow microcapsules presented a $CO_2$ sorption capacity of 49 $mgCO_2.g^{-1}$, 38 $mgCO_2.g^{-1}$ and 27 $mgCO_2.g^{-1}$, respectively, as seen in $CO_2$ capture tests performed at 45 °C and 0.5 MPa of pressure [61]. In summarizing, the best sorption results of the present work were achieved with encapsulated ILs [emim][$Tf_2N$] with the highest ILs concentration M40-Tf2N, 33.6 % (w/ w), (sorption capacity: 49.2 ± 1.1 $mgCO_2.g^{-1}$) while the best sorption results for the microcapsules containing the ILs [emim][TfO] was obtained for M15-TfO, 13 % (w/w), (sorption capacity: 53 ± 0.9 $mgCO_2.g^{-1}$).

As previously seen, $CO_2$ sorption results indicate that good sorption values can be achieved with capsules with low ILs concentrations (M15-TfO) and higher IL concentrations (M40-$Tf_2N$). To further study microcapsule $CO_2/N_2$ selectivity samples with lower and higher IL content were selected (see Fig. 8). The selectivity of the pristine acrylic polymer (microcapsules shell material) was first evaluated (2.3 ± 0.2). Samples M15-Tf2N and M40-Tf2N presented similar selectivity values, 3.9 ± 0.2 and 3.8 ± 0.15, respectively. The lower IL content (12.3 w/w %) of sample M15-$Tf_2N$ makes it a good candidate for $CO_2$ capture taking into consideration the higher IL costs compared to the acrylic-based shell. For $CO_2$ selectivity of microcapsules M15-TfO (4.5 ± 0.2) and M40-TfO (3.3 ± 0.2), the same behavior observed for $CO_2$ sorption capacity was repeated for $CO_2/N_2$ selectivity with the sample containing lower IL content presenting the best performance. M15-TfO (13 % (m/m) presented the best $CO_2$ sorption capacity (53 ± 0.9 $mgCO_2.g^{-1}$) and selectivity (4.5 ± 0.2) among all microcapsules evaluated in this work. When compared to the pristine acrylic shell the selectivity of M15-TfO is 95 % superior indicating the synergetic effect of the IL/Shell. In addition to the sorption and selectivity tests, the $CO_2$ sorption kinetics of M15-TfO was performed (Fig. 10). The percentage of $CO_2$ saturation in the sample increases exponentially, with an 88 % increase observed in less than one minute. After 5.8 min, the sample reaches 100 % $CO_2$ saturation (53 ± 0.9 mg $CO_2.g^{-1}$ sorption). Our research group previously reported [12], that ionic liquids in liquid form can take over 40 min to reach 100 % saturation in sorption tests. This behavior has been observed by other research groups as well, confirming the kinetics of neat IL to be consistent with our findings [63–65]. This data provides valuable insight into the sorption behavior of microcapsules and suggests that they could be used as an effective means of separating $CO_2$ from other gases. The results show that the microcapsules have a fast $CO_2$ sorption rate and a high $CO_2$ capacity, indicating that they are capable of efficiently capturing $CO_2$ from gas mixtures.

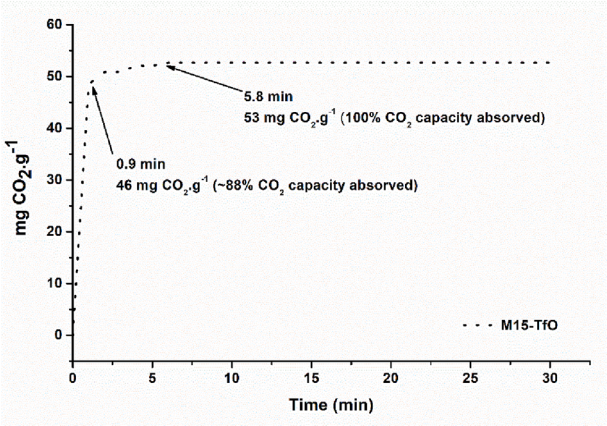


**Fig. 10.** Kinetic $CO_2$ sorption curve of M15-TfO. The percentage sorption values refer to the total $CO_2$ sorption capacity of the sample (53 ± 0.9 $mgCO_2.g^{-1}$), as reported in Fig. 9, and the respective test duration. The test conditions were the same as those used in the $CO_2$ sorption tests (45 °C and 0.4 MPa).

### 3.6. FESEM and EDS analysis

Microcapsules morphology of samples containing lower and higher IL content was evaluated by FESEM and the composition by EDS. The M15-TfO (Fig. 11) presents some regions with agglomerated microcapsules, however, well-defined and separated microcapsules prevail presenting an average particle size of 60 μm. Increasing IL content (M40-TfO) resulted in larger (diameter = 75 μm ± 1.3) and agglomerated microcapsules. This behavior is probably due to the higher IL content during the encapsulation step. M15-Tf2N (diameter = 80 μm ± 0.8) and M40-Tf2N (diameter = 57 μm ± 1.8) presented similar behaviors, resulting in well-formed microcapsules when using lower IL content. Microcapsules size and the IL content influence $CO_2$ sorption capacity indicating that samples combining a lower % of encapsulated IL and smaller particle diameter, as seen in the case of sample M15-TfO (53 ± 0.9 $mgCO_2.g^{-1}$ and selectivity 4.5 ± 0.2), provide better results. Microcapsules EDS analysis evidences the presence of fluorine and sulfur characteristic of the anions present in the ILs, indicating their effective encapsulation.

### 3.7. Sorption/desorption cycles tests

M15-TfO presented the best $CO_2$ sorption ability and $CO_2/N_2$ selectivity being selected to study sample stability during sorption/desorption cycles. Five sorption/desorption cycles were performed, and $CO_2$ sorption capacity was constant as seen in Fig. 12. This result shows microcapsule stability allowing the use in continuous capture processes.

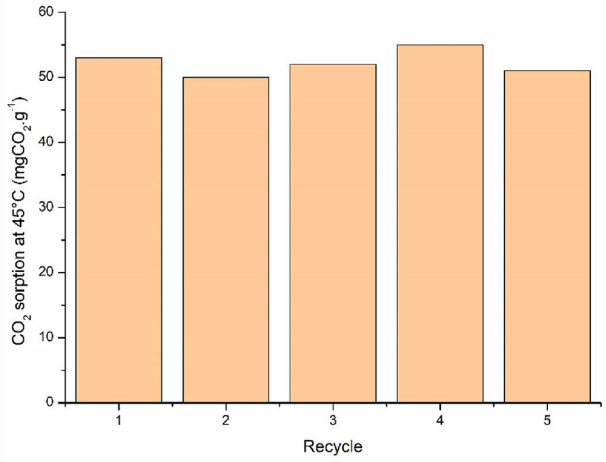


**Fig. 12.** The sorption and desorption cycles tests realized in the sample, M15-TfO, that had the best $CO_2$ sorption and $CO_2/N_2$ selectivity: five tests were performed to ensure the $CO_2$ sorption capacity stability from the sample.

### 3.8. DFT analysis

To rationalize the above-reported experimental results, we used electronic-structure calculations. The systems consisted of one to four ion pairs, one $CO_2$ molecule, and one $N_2$ molecule. Larger systems were used to verify the trends obtained for a single ion pair. The goal of these simulations was to identify all stationary points located on the respective potential energy surfaces that are responsible for gas adsorption by ionic liquids [emim][$Tf_2N$] and [emim][TfO]. Both scavengers capture gases thanks to the electrostatic attraction in the case of $CO_2$ and van der Waals attraction in the case of $N_2$ (physisorption mechanisms). It is essential to in silico represent the same system components as in the experiment since the competitive coordination of particles plays a paramount role in the overall sorption. In particular, the $Tf_2N$ and TfO anions and the $CO_2$ molecule compete for the location in the vicinity of the intrinsically acidic hydrogen atom in the imidazole ring, H—C2. Analogously, the emim cation competes with the $CO_2$ molecule to appear in the stationary point corresponding to their coordinations by one of the oxygen atoms (these binding sites are conventionally denoted as "OS") of the employed anions. The exclusion of any above-mentioned elements from an electronic-structure simulation would drastically alter the potential energy surface and lead to biased results.

Dinitrogen is a notably thermodynamically stable and non-polar molecule. It possesses a relatively large dispersion constant and can, therefore, adsorb on either non-polar surfaces or surfaces with tight packing of atoms, e.g., activated carbon species. The current simulations were used to probe the stationary points which correspond to the adsorption of $N_2$ by [emim][$Tf_2N$] and [emim][TfO]. Since $CO_2$ and $N_2$ exhibit different types of electronic density distribution, they are unlikely to compete for the same binding sites.

Fig. 13 depicts a series of ion-molecular configurations involving

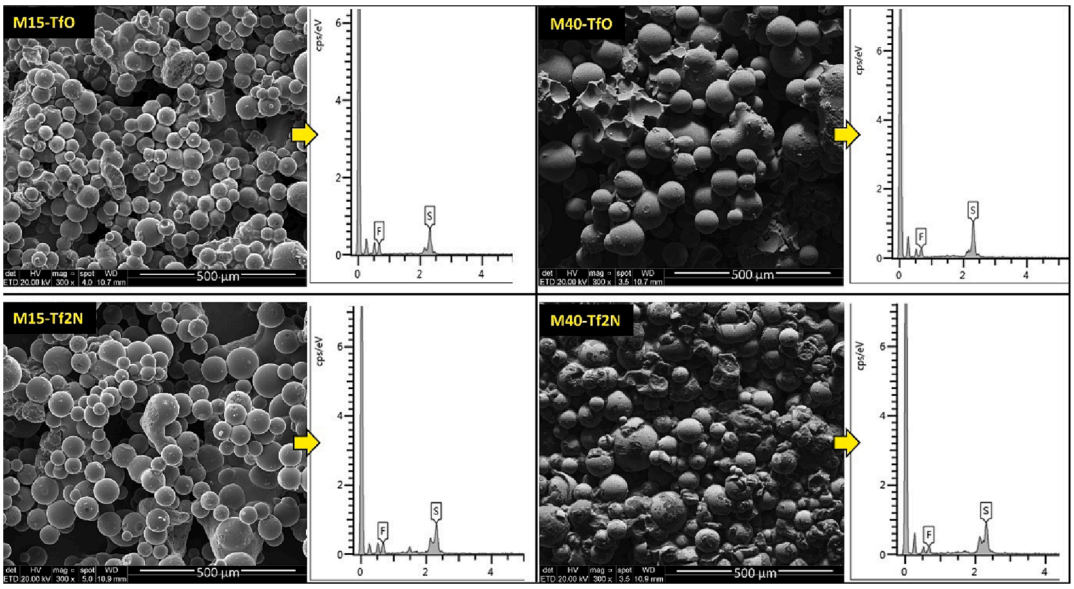


**Fig. 11.** Field emission scanning electron microscopy (FESEM) and energy dispersion mapping X-ray spectrometry (EDS) of microcapsules with the highest and lowest IL concentration, the influence of percent mass of ionic liquid microencapsulated over the morphological changes in the microcapsules and the presence of characteristic ionic liquids elements are showed.

$CO_2$, $N_2$, and [emim][TfO], whereas Table 2 provides certain descriptors of them. The cation–anion coordination patterns dominate the potential energy surface and correspond to the lowest formation enthalpies of the systems. This is rather expected because of the well-known strong electrostatic attraction between the H(—C2) atom of emim and the electron-rich sites of many anions. In the case of [emim][TfO], the H(C2)—OS spatial correlation is seen. Consider the corresponding closest-approach cation–anion distances of 0.207, 0.205, 0.185, 0.212, and 0.193 nm. Based on the lengths and the obtuse C—H…O angles (103–139°), all but the fourth one (distance of 0.214 nm and angle of 84°) out of the detected configurations are medium-strength hydrogen bonds. The above-enumerated values were arranged according to the total potential energy of the system. It is noteworthy that the tightest cation–anion coordination does not necessarily correspond to the lowest overall potential energy.

Due to a strong cation–anion coupling exemplified above, the $CO_2$ molecule is unable to coordinate an intrinsically acidic hydrogen atom in the imidazole ring. This result once again underlines the principal incorrectness of earlier reports in which the simulations did not include anion. To consider the imidazole hydrogen as a potential adsorption site for $CO_2$, a more weakly coordinating anion than TfO is urged. Instead of imidazole hydrogen, we revealed that the sulfur-linked oxygen atoms of TfO hold promise to attract the carbon atom of $CO_2$ via the interaction of their electric moments. The C($CO_2$)—O(TfO) distances equal 0.235, 0.233, 0.233, 0.231, and 0.285 nm provided in the order of decreasing system standard formation enthalpies (Table 2). Larger partial chargers on the oxygen atoms generally correlate with tighter coordination of $CO_2$ in this region of space. We hereby conclude that the oxygen atoms of TfO represent primary drivers of $CO_2$ physisorption by [emim][TfO], whereas an anticipated role of [emim] appeared unreasonably overestimated.

Concerning $N_2$, we did not find any articulated adsorption site for this molecule. The inability of [emim][TfO] to capture $N_2$ sounds favorable for the applications of the proposed systems in gas separation. Dinitrogen locates 0.265 nm far from H(—C5) of the imidazole ring in the global minimum configuration. In state II with a standard system formation enthalpy of −1341 kJ/mol (see Table 3), the closest-approach distance between $N_2$ and [emim][TfO] amounts to 0.265 nm. Hereby dinitrogen locates near the oxygen atom of TfO and about 0.9 nm far from H(—C5). In other configurations, the location of $N_2$ in the vicinity of the trifluoromethyl moiety (N—F distance is 0.323 nm) was also detected. All the enumerated interactions are weak dispersion binding. The absence of one or two specific binding destinations for $N_2$ indicates an inability of [emim][TfO] to scavenge dinitrogen.

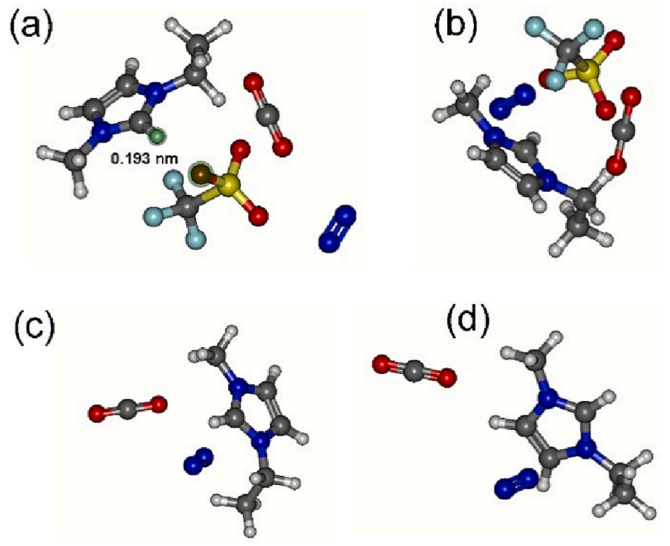


**Fig. 13.** The most representative ion-molecular configurations corresponding to the competitive sorption of $CO_2$ and $N_2$ by [emim][TfO]: (a) the cation–anion approach distance, r (O, TfO–H,emim) = 0.193 nm; (b) the global minimum configuration, r (cation–anion) = 0.207 nm; (c) $N_2$ near the ethyl side chain of emim; (d) $CO_2$ and $N_2$ close to the cation. Note that all depicted configurations represent minima on the potential energy surface. Carbons are grey, hydrogens are white, nitrogens are blue, oxygens are red, fluorines are cyan, and sulfur is yellow.

Fig. 14 summarizes a few noteworthy ion-molecular arrangements corresponding to the stationary points detected in the [emim][$Tf_2N$] + $CO_2$ + $N_2$ system. Table 3, in turn, provides specific descriptors in these states. Since [emim][$Tf_2N$] is more geometrically flexible than [emim][TfO], the number of its stationary points is also somewhat larger. Note that we provide only the most representative stationary points in all systems to underline the diversity of the investigated chemical compositions and reflect the most probable coordination patterns. In all cases, the global minimum states are reported and essentially characterized since the latter is expected to influence the real-world behavior of each system to the largest extent.

In [emim][$Tf_2N$], the cation–anion coordination is less tight as compared to the above-considered case of [emim][TfO]. In certain cases, $CO_2$ occupies a position near the acidic imidazole hydrogen atom. Yet, the most thermodynamically stable configurations, are characterized by preferential cation–anion binding. For instance, in the state I (global minimum), the H(—C2)—O(—S) distances are 0.206 and 0.209 nm. The C—H…O angles are 142 and 133°, respectively. The formation of two medium-strength bonds in this sample essentially stabilizes an ionic subsystem of [emim][$Tf_2N$] + $CO_2$ + $N_2$. In turn, $CO_2$ approaches an imidazole acidic oxygen by 0.236 nm. Given the C—H…O angles of 107°, such interaction can be designated as a very weak hydrogen bonding. Similar to the case of [emim][TfO], a substantial electrostatic attraction between the carbon atom of carbon dioxide and one of the oxygen atoms of $Tf_2N$ results in a stationary point with a non-covalent separation of 0.236 nm.

Dinitrogen exhibits preferential locations above the imidazole ring. The cation-$N_2$ closest-approach distances of 0.246 and 0.257 nm were recorded in various stationary points. These distances correspond to nitrogen near methylene and methyl moieties of the cation's side chains. In the vicinity of the $Tf_2N$ anion, $N_2$ prefers the locations near oxygen atoms, viz., distances of 0.265, 0.268, and 0.271 nm in low-energy stationary points.

The comparison between $N_2$-[emim][$Tf_2N$]/[emim][TfO] and $CO_2$-[emim][$Tf_2N$]/[emim][TfO] contributes valuable information to rationalize the experimentally selectivities. The intercomponent binding energies (Table 3) represent an important physical property that can exclusively be derived from theoretical modeling. In the global minimum states, the ratios of $CO_2/N_2$ binding energies amount to 9.8 in [emim][TfO] and 3.9 in [emim][$Tf_2N$]. Compare these to the experimentally determines selectivities ranging from three to five in various samples comprising both the ionic liquids and the polymeric components. Since the comparison performed is indirect, i.e., between different properties, the observed agreement can be considered trustworthy. According to the simulations, [emim][$Tf_2O$] must be an ionic liquid of choice for $CO_2/N_2$ separation applications. However, this has not been convincingly confirmed by the experiments which reveal a noisy trend. Additional experimentation might be required to shape out the difference predicted in silico.

It is noteworthy that binding energies greatly depend on the considered stationary point of the sample and do not correlate with the energy-based order of the stationary points on the potential energy surfaces. For instance, the largest $CO_2/N_2$ ratio amounts to 19. It is observed in state III of the [emim][TfO] + $CO_2$ + $N_2$ system. The lowest $CO_2/N_2$ ratio amounts to 1.2. It is observed in state VI of the [emim][$Tf_2N$] + $CO_2$ + $N_2$ system. Note that the probability of each state implementation in a real-world system depends on its formation enthalpy (Table 3). A lower enthalpy means that the system spends more time in the respective microscopic state. Interestingly, the higher-energy

**Table 3**
The stationary points, their formation energies, gas adsorption energies, and selected electrostatic charges on the detected binding sites of [emim][TfO] and [emim][$Tf_2N$]. The energies are provided per mole of a $CO_2/N_2$ gas.

| Ionic liquid | Point, # | Hform, kJ/mol | Eb ($N_2$–X) kJ/mol | Eb ($CO_2$–X) kJ/mol | q($H_2$), e | q(O)*, e | q(F)*, e |
|---|---|---|---|---|---|---|---|
| [emim] | I | −1346 | 3.05 | 29.8 | +0.29 | −0.59 | −0.14 |
| [TfO] | II | −1341 | 2.22 | 28.5 | +0.29 | −0.62 | −0.13 |
| | III | −1334 | 1.42 | 27.4 | +0.28 | −0.59 | −0.20 |
| | IV | −1321 | 4.64 | 30.8 | +0.29 | −0.61 | −0.16 |
| | V | −1308 | 4.68 | 30.8 | +0.29 | −0.61 | −0.16 |
| [emim] | I | −2128 | 5.94 | 23.3 | +0.25 | −0.56 | −0.10 |
| [$Tf_2N$] | II | −2124 | 12.7 | 22.6 | −0.11 | −0.47 | −0.12 |
| | III | −2120 | 12.8 | 22.0 | −0.03 | −0.50 | −0.12 |
| | IV | 2116 | 10.7 | 22.4 | +0.11 | −0.53 | −0.12 |
| | V | −2108 | 6.15 | 16.7 | +0.18 | −0.58 | −0.13 |
| | VI | −2103 | 8.74 | 10.5 | +0.22 | −0.51 | −0.14 |
| | VII | −2074 | 8.28 | 12.0 | +0.22 | −0.45 | −0.15 |

* Maximum absolute charge is provided.

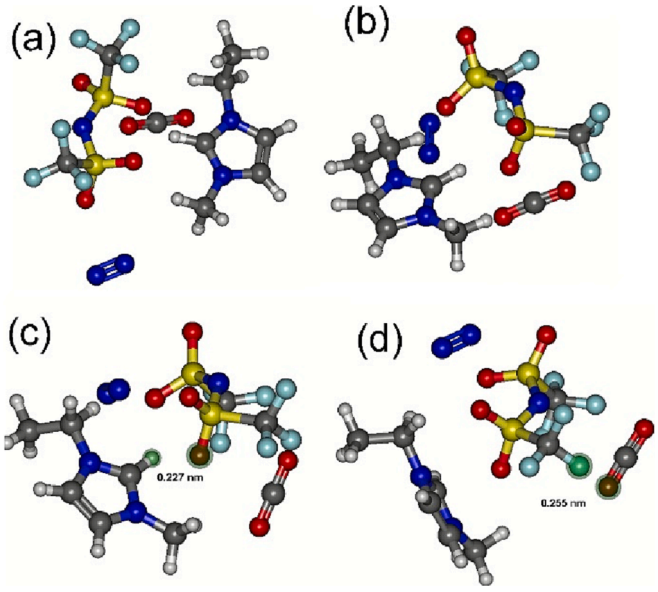


**Fig. 14.** The most representative ion-molecular configurations corresponding to the competitive sorption of $CO_2$ and $N_2$ by [emim][TfN]: (a) $CO_2$ locates near the oxygen atom of $Tf_2N$ (distance of 0.238 nm) and the $C_2$ hydrogen atom of emim (distance of 0.246 nm) simultaneously, the global minimum configuration; (b) $CO_2$ coordinates one of the oxygen atoms of $Tf_2N$; (c) a strong cation–anion coupling; (d) $CO_2$ coordinates the trifluoromethyl moiety of $Tt_2N$. Note that all depicted configurations represent minima on the potential energy surface. Carbons are grey, hydrogens are white, nitrogens are blue, oxygens are red, fluorines are cyan, and sulfur is yellow.

states corresponding to both ionic liquids favor smaller differences between $CO_2$ and $N_2$ adsorption energies. The simulations clearly indicated that the most thermodynamically stable states of each system are driven by strong cation–anion coordination rather than the adsorption of the $CO_2/N_2$ gas molecules. The usage of weaker coordinating cations and/or anions can increase both $CO_2$ sorption and $CO_2/N_2$ selectivity.

## 4. Conclusions

The suspension encapsulation methodology was successfully used in the production of [emim][TfO] and [emim][$Tf_2N$] (core) acrylic-based (shell) microcapsules as shown by the different characterization techniques. The encapsulation efficiency was greater than 80 % corroborating the encapsulation process efficiency. Infrared and EDS analyses confirmed the IL presence in microcapsules and TEM evidenced the polynuclear morphology. Small fusion regions shown in DSC analysis and attributed to the IL also corroborate microcapsule formation by combining amorphous acrylic polymer with IL. The evaluation of the ideal amount of IL and the influence of the anion type in the microcapsules showed that lower [emim][TfO] concentrations result in the formation of microcapsules with greater affinity for the $CO_2$ molecule when compared to M40-$Tf_2N$. Electronic structure modeling corroborated the experimental results proving that [emim][TfO] is better to separate $CO_2/N_2$ thanks to three electron-rich oxygens evidencing also that [emim] is not essential. The lower $CO_2$ selectivity of capsules with $Tf_2N$ is also clarified showing that fluoromethyl slightly increases affinity to $N_2$ decreasing $CO_2$ selectivity. Yet, the produced samples are stable during sorption/desorption tests proving to be candidates to be evaluated in industrial post-combustion capture processes.

## CRediT authorship contribution statement

**Rafael Duczinski:** Conceptualization, Methodology, Investigation. **Barbara B. Polesso:** Methodology, Investigation. **Evandro Duarte:** Investigation, Validation. **Franciele L. Bernard:** Conceptualization, Investigation, Methodology. **Vitaly V. Chaban:** Conceptualization, Methodology, Investigation. **Sandra Einloft:** Conceptualization, Methodology, Project administration, Funding acquisition.

## Declaration of Competing Interest

The authors declare that they have no known competing financial interests or personal relationships that could have appeared to influence the work reported in this paper.

## Data availability

Data will be made available on request.

## Acknowledgments

The authors acknowledge support from Fapergs (21/2551-0002235-3) and Shell Brazil and the strategic importance of the support provided by the ANP (Brazil's National Oil, Natural Gas, and Biofuels Agency) through the R&D levy regulation. Sandra Einloft thanks CNPq for her research scholarship. Rafael Duczinski and Barbara B. Polesso thank CAPES for their Ph.D. scholarship. This study was financed in part by the Coordenação de Aperfeiçoamento de Pessoal de Nível Superior – Brasil (CAPES) – Finance Code 001.

## References

[1] A. Melelli, S. Durand, C. Alvarado, A. Kervoëlen, L. Foucat, M. Grégoire, O. Arnould, X. Falourd, F. Callebert, P. Ouagne, A. Geairon, S. Daniel, F. Jamme, C. Mauve, B. Gakière, A. Bourmaud, J. Beaugrand, Anticipating global warming effects: a comprehensive study of drought impact of both flax plants and fibres, Ind. Crop. Prod. 184 (2022), 115011, https://doi.org/10.1016/j.indcrop.2022.115011.

[2] S.I. Zandalinas, F.B. Fritschi, R. Mittler, Global warming, climate change, and environmental pollution: recipe for a multifactorial stress combination disaster, Trends Plant Sci. 26 (2021) 588–599, https://doi.org/10.1016/j.tplants.2021.02.011.

[3] Q. Yirong, Does environmental policy stringency reduce CO2 emissions? Evidence from high-polluted economies, J. Clean. Prod. 341 (2022), 130648, https://doi.org/10.1016/j.jclepro.2022.130648.

[4] A.A. Al-absi, M. Mohamedali, A. Domin, A.M. Benneker, N. Mahinpey, Development of in situ polymerized amines into mesoporous silica for direct air CO 2 capture, Chem. Eng. J. 447 (2022), 137465, https://doi.org/10.1016/j.cej.2022.137465.

[5] A. Balraj, A.P.C. Sekaran, N. Ramamurthy, R. Babarao, K.K. Nagarajan, S. A. Mayilvahanan, Systematic review on sono-assisted CO2 stripping, solvent recovery and energy demand aspects in solvent-based post-combustion carbon dioxide capture process, Chem. Eng. Process. - Process Intesif. 170 (2022), 108723, https://doi.org/10.1016/j.cep.2021.108723.

[6] B. Yuan, G. Zhan, Z. Chen, Y. Li, L. Wang, C. You, J. Li, Intrinsic insight of energy-efficiency optimization for CO2 capture by amine-based solvent: effect of mass transfer and solvent regeneration, Int. J. Greenhouse Gas Control 118 (2022), 103673, https://doi.org/10.1016/j.ijggc.2022.103673.

[7] W. Jiang, X. Li, G. Gao, F. Wu, C. Luo, L. Zhang, Advances in applications of ionic liquids for phase change CO2 capture, Chem. Eng. J. 445 (2022), 136767, https://doi.org/10.1016/j.cej.2022.136767.

[8] M. Akram, K. Milkowski, J. Gibbins, M. Pourkashanian, Controlling capture plants to avoid CO2 emissions penalties during peak load demand, Int. J. Greenhouse Gas Control 106 (2021), 103285, https://doi.org/10.1016/j.ijggc.2021.103285.

[9] A. Gutierrez-Ortega, R. Nomen, J. Sempere, J.B. Parra, M.A. Montes-Morán, R. Gonzalez-Olmos, A fast methodology to rank adsorbents for CO2 capture with temperature swing adsorption, Chem. Eng. J. 435 (2022) 15–17, https://doi.org/10.1016/j.cej.2022.134703.

[10] D. Hospital-Benito, J. Lemus, C. Moya, R. Santiago, J. Palomar, Improvement of CO2 capture processes by tailoring the reaction enthalpy of Aprotic N-Heterocyclic anion-based ionic liquids, Chem. Eng. J. Adv. 10 (2022), 100291, https://doi.org/10.1016/j.ceja.2022.100291.

[11] N.S. Matin, W.P. Flanagan, Life cycle assessment of amine-based versus ammonia-based post combustion CO2 capture in coal-fired power plants, Int. J. Greenhouse Gas Control 113 (2022), 103535, https://doi.org/10.1016/j.ijggc.2021.103535.

[12] F.L. Bernard, E.A. Duarte, B.B. Polesso, R.B. Duczinski, S. Einloft, CO2 sorption using encapsulated imidazolium-based fluorinated ionic liquids, Environ. Chall. 4 (2021), 100109, https://doi.org/10.1016/j.envc.2021.100109.

[13] X. (Eric) Hu, L. Liu, X. Luo, G. Xiao, E. Shiko, R. Zhang, X. Fan, Y. Zhou, Y. Liu, Z. Zeng, C. Li, A review of N-functionalized solid adsorbents for post-combustion CO2 capture, Appl. Energy 260 (2020), 114244, https://doi.org/10.1016/j.apenergy.2019.114244.

[14] K. Wu, S. Deng, S. Li, R. Zhao, X. Yuan, L. Zhao, Preliminary experimental study on the performance of CO2 capture prototype based on temperature swing adsorption (TSA), Carbon Capt. Sci. Technol. 2 (2022), 100035, https://doi.org/10.1016/j.ccst.2022.100035.

[15] D.M. Rodrigues, F. Bernard, C. Le Roux, E. Duarte, Synthetic silico-metallic mineral particles SSMMP: a new option for CO 2 capture and CO 2/N 2 separation from post-combustion technology, Appl. Clay Sci. 226 (2022), 106572, https://doi.org/10.1016/j.clay.2022.106572.

[16] M. Bermeo, L.F. Vega, M.R.M. Abu-Zahra, M. Khaleel, Critical assessment of the performance of next-generation carbon-based adsorbents for CO2 capture focused on their structural properties, Sci. Total Environ. 810 (2022), 151720, https://doi.org/10.1016/j.scitotenv.2021.151720.

[17] R. Duczinski, B.B. Polesso, F.L. Bernard, H.Z. Ferrari, P.L. Almeida, M.C. Corvo, E. J. Cabrita, S. Menezes, S. Einloft, Enhancement of CO2/N2 selectivity and CO2 uptake by tuning concentration and chemical structure of imidazolium-based ILs immobilized in mesoporous silica, J. Environ. Chem. Eng. 8 (2020), 103740, https://doi.org/10.1016/j.jece.2020.103740.

[18] A. Shohrat, M. Zhang, H. Hu, X. Yang, L. Liu, H. Huang, Mechanism study on CO2 capture by ionic liquids made from TFA blended with MEA and MDEA, Int. J. Greenhouse Gas Control 119 (2022), 103709, https://doi.org/10.1016/j.ijggc.2022.103709.

[19] H. Wang, J. Zhu, L. Tan, M. Zhou, S. Zhang, Encapsulated ionic liquids for CO2 capture, Mater. Chem. Phys. 251 (2020), 122982, https://doi.org/10.1016/j.matchemphys.2020.122982.

[20] J. Lemus, F.A. Da Silva, J. Palomar, P.J. Carvalho, J.A.P. Coutinho, Solubility of carbon dioxide in encapsulated ionic liquids, Sep. Purif. Technol. 196 (2018) 41–46, https://doi.org/10.1016/j.seppur.2017.08.032.

[21] L. Nie, Y. Mu, J. Jin, J. Chen, J. Mi, Recent developments and consideration issues in solid adsorbents for CO2 capture from flue gas, Chin. J. Chem. Eng. 26 (2018) 2303–2317, https://doi.org/10.1016/j.cjche.2018.07.012.

[22] M. Pardakhti, T. Jafari, Z. Tobin, B. Dutta, E. Moharreri, N.S. Shemshaki, S. Suib, R. Srivastava, Trends in solid adsorbent materials development for CO2 capture, ACS Appl. Mater. Interfaces 11 (2019) 34533–34559, https://doi.org/10.1021/acsami.9b08487.

[23] M.E. Potter, K.M. Cho, J.J. Lee, C.W. Jones, Role of alumina basicity in CO2 uptake in 3-aminopropylsilyl-grafted alumina adsorbents, ChemSusChem. 10 (2017) 2192–2201, https://doi.org/10.1002/cssc.201700115.

[24] F.L. Bernard, B.B. Polesso, F.W. Cobalchini, V.V. Chaban, J.F. Do Nascimento, F. Dalla Vecchia, S. Einloft, Hybrid alkoxysilane-functionalized urethane-imide-based poly(ionic liquids) as a new platform for carbon dioxide capture, Energy Fuel 31 (2017) 9840–9849, https://doi.org/10.1021/acs.energyfuels.7b02027.

[25] F.L. Bernard, R.B. Duczinski, M.F. Rojas, M.C.C. Fialho, L.Á. Carreño, V.V. Chaban, F.D. Vecchia, S. Einloft, Cellulose based poly(ionic liquids): tuning cation-anion interaction to improve carbon dioxide sorption, Fuel 211 (2018) 76–86, https://doi.org/10.1016/j.fuel.2017.09.057.

[26] J.K. Stolaroff, C. Ye, J.S. Oakdale, S.E. Baker, W.L. Smith, D.T. Nguyen, C. M. Spadaccini, R.D. Aines, Microencapsulation of advanced solvents for carbon capture, Faraday Discuss. 192 (2016) 271–281, https://doi.org/10.1039/C6FD00049E.

[27] J.M. Knipe, K.P. Chavez, K.M. Hornbostel, M.A. Worthington, D.T. Nguyen, C. Ye, W.L. Bourcier, S.E. Baker, J.F. Brennecke, J.K. Stolaroff, Evaluating the performance of micro-encapsulated CO2 sorbents during CO2 absorption and regeneration cycling, Environ. Sci. Tech. 53 (2019) 2926–2936, https://doi.org/10.1021/acs.est.8b06442.

[28] A. Jamekhorshid, S.M. Sadrameli, M. Farid, A review of microencapsulation methods of phase change materials (PCMs) as a thermal energy storage (TES) medium, Renew. Sustain. Energy Rev. 31 (2014) 531–542, https://doi.org/10.1016/j.rser.2013.12.033.

[29] Q. Luo, Y. Wang, Z. Chen, P. Wei, E. Yoo, E. Pentzer, Pickering emulsion-templated encapsulation of ionic liquids for contaminant removal, ACS Appl. Mater. Interfaces 11 (2019) 9612–9620, https://doi.org/10.1021/acsami.8b21881.

[30] G.R. Guillen, Y. Pan, M. Li, E.M.V. Hoek, Preparation and characterization of membranes formed by nonsolvent induced phase separation: a review, Ind. Eng. Chem. Res. 50 (2011) 3798–3817, https://doi.org/10.1021/ie101928r.

[31] Y.Y. Lee, K. Edgehouse, A. Klemm, H. Mao, E. Pentzer, B. Gurkan, Capsules of reactive ionic liquids for selective capture of carbon dioxide at low concentrations, ACS Appl. Mater. Interfaces 12 (2020) 19184–19193, https://doi.org/10.1021/acsami.0c01622.

[32] Y. Zhang, Z. Wu, S. Chen, P. Yu, Y. Luo, CO2 capture by imidazolate-based ionic liquids: effect of functionalized cation and dication, Ind. Eng. Chem. Res. 52 (2013) 6069–6075, https://doi.org/10.1021/ie302928v.

[33] A. Finotello, J.E. Bara, D. Camper, R.D. Noble, Room-temperature ionic liquids: temperature dependence of gas solubility selectivity, Ind. Eng. Chem. Res. 47 (2008) 3453–3459, https://doi.org/10.1021/ie0704142.

[34] E.R. Parnham, R.E. Morris, 1-Alkyl-3-methyl imidazolium bromide ionic liquids in the ionothermal synthesis of aluminium phosphate molecular sieves, Chem. Mater. 18 (2006) 4882–4887, https://doi.org/10.1021/cm0615929.

[35] Y. Ma, Z. Li, H. Wang, H. Li, Synthesis and optimization of polyurethane microcapsules containing [BMIm]PF6 ionic liquid lubricant, J. Colloid Interface Sci. 534 (2019) 469–479, https://doi.org/10.1016/j.jcis.2018.09.059.

[36] R. Duczinski, F. Bernard, M. Rojas, E. Duarte, V. Chaban, F.D. Vecchia, S. Menezes, S. Einloft, Waste derived MCMRH- supported IL for CO2/CH4 separation, J. Nat. Gas Sci. Eng. 54 (2018) 54–64, https://doi.org/10.1016/j.jngse.2018.03.028.

[37] W. Span, R. Wagner, A new EOS for CO2 covering the fluid region from the triple point temperature to 1100K at pressures up to 800MPa.pdf, J. Phys. Chem. Ref. Data 25 (1996) 1509–1596, https://doi.org/10.1063/1.555991.

[38] R. Peverati, D.G. Truhlar, Improving the accuracy of hybrid meta-GGA density functionals by range separation, J. Phys. Chem. Lett. 2 (2011) 2810–2817, https://doi.org/10.1021/jz201170d.

[39] V.V. Chaban, Diethyl sulfoxide as a novel neutral ligand in the platinum complex compound, Comput. Theor. Chem. 1211 (2022), 113683, https://doi.org/10.1016/j.comptc.2022.113683.

[40] V.V. Chaban, N.A. Andreeva, Mutual miscibility of diethyl sulfoxide and acetonitrile: fundamental origin, J. Mol. Liq. 349 (2022), 118110, https://doi.org/10.1016/j.molliq.2021.118110.

[41] J.J.P. Stewart, Application of the PM6 method to modeling proteins, J. Mol. Model. 15 (2009) 765–805, https://doi.org/10.1007/s00894-008-0420-y.

[42] J.J.P. Stewart, Optimization of parameters for semiempirical methods VI: more modifications to the NDDO approximations and re-optimization of parameters, J. Mol. Model. 19 (2013) 1–32, https://doi.org/10.1007/s00894-012-1667-x.

[43] V.V. Chaban, N.A. Andreeva, Sodium-ion electrolytes based on ionic liquids: a role of cation-anion hydrogen bonding, J. Mol. Model. 22 (2016), https://doi.org/10.1007/s00894-016-3042-9.

[44] V.V. Chaban, N.A. Andreeva, Solvation of the morpholinium cation in acetonitrile. Effect of an anion, J. Mol. Model. 22 (2016) 1–8, https://doi.org/10.1007/s00894-015-2896-6.

[45] M.W. Schmidt, K.K. Baldridge, J.A. Boatz, S.T. Elbert, M.S. Gordon, J.H. Jensen, S. Koseki, N. Matsunaga, K.A. Nguyen, S. Su, T.L. Windus, M. Dupuis, J. A. Montgomery, General atomic and molecular electronic structure system, J. Comput. Chem. 14 (1993) 1347–1363, https://doi.org/10.1002/jcc.540141112.

[46] V. Chaban, Annealing relaxation of ultrasmall gold nanostructures, Chem. Phys. Lett. 618 (2015) 46–50, https://doi.org/10.1016/j.cplett.2014.10.070.

[47] A. Allouche, Software news and updates Gabedit — a graphical user interface for computational chemistry softwares, J. Comput. Chem. 32 (2012) 174–182, https://doi.org/10.1002/jcc.21600.

[48] J.K. Stolaro, C. Ye, J.S. Oakdale, S.E. Baker, W.L. Smith, D.T. Nguyen, C.M. Spadaccini, R.D. Aines, Microencapsulation of advanced solvents for carbon capture, 2016, pp. 271–281, doi: 10.1039/C6FD00049E.

[49] J.J. Vericella, S.E. Baker, J.K. Stolaroff, E.B. Duoss, J.O. Hardin, J. Lewicki, E. Glogowski, W.C. Floyd, C.A. Valdez, W.L. Smith, J.H. Satcher, W.L. Bourcier, C. M. Spadaccini, J.A. Lewis, R.D. Aines, Encapsulated liquid sorbents for carbon dioxide capture, Nat. Commun. 6 (2015) 1–7, https://doi.org/10.1038/ncomms7124.

[50] A.N. Soriano, B.T. Doma, M.H. Li, Carbon dioxide solubility in 1-ethyl-3-methylimidazolium trifluoromethanesulfonate, J. Chem. Thermodyn. 41 (2009) 525–529, https://doi.org/10.1016/j.jct.2008.11.001.

[51] D.D. Ferreyra, N.M. Correa, J.J. Silber, R.D. Falcone, The effect of different interfaces and confinement on the structure of the ionic liquid 1-butyl-3-methylimidazolium bis(trifluoromethylsulfonyl)imide entrapped in cationic and anionic reverse micelles, PCCP 14 (2012) 3460–3470, https://doi.org/10.1039/c2cp23481e.
[52] S.H. Liu, C.C. Chen, B. Zhang, J.H. Wu, Fire and explosion hazards of 1-ethyl-3-methylimidazolium bis(trifluoromethylsulfonyl)imide, RSC Adv. 10 (2020) 22468–22479, https://doi.org/10.1039/d0ra01821j.
[53] N.A.S.N. Zulkepeli, T. Winie, R.H.Y. Subban, Infrared studies of PVC-based electrolytes incorporated with lithium triflate and 1-butyl-3-methyl imidazolium trifluoromethanesulfonate as ionic liquid, AIP Conf. Proc. 2017 (1877) 1–8, https://doi.org/10.1063/1.4999880.
[54] J. Dong, Y. Ozaki, FTIR and FT-Raman studies of partially miscible poly(methyl methacrylate)/poly(4-vinylphenol) blends in solid states, Macromolecules 30 (1997) 286–292, https://doi.org/10.1021/ma9607168.
[55] L.M. Ramenskaya, E.P. Grishina, Intensification phenomenon of weak ionic interactions of 1-butyl-3-methylimidazolium hexafluorophosphate ionic liquid macro-dispersed in poly(methyl methacrylate): FTIR spectroscopic evidence, J. Mol. Liq. 218 (2016) 133–137, https://doi.org/10.1016/j.molliq.2016.02.037.
[56] S. Sanghi, E. Willett, C. Versek, M. Tuominen, E.B. Coughlin, Physicochemical properties of 1,2,3-triazolium ionic liquids, RSC Adv. 2 (2012) 848–853, https://doi.org/10.1039/c1ra00286d.
[57] I. Bandrés, F.M. Royo, I. Gascón, M. Castro, C. Lafuente, Anion influence on thermophysical properties of ionic liquids: 1-butylpyridinium tetrafluoroborate and 1-butylpyridinium triflate, J. Phys. Chem. B 114 (2010) 3601–3607, https://doi.org/10.1021/jp9120707.
[58] M. Peanparkdee, S. Iwamoto, R. Yamauchi, Microencapsulation: a review of applications in the food and pharmaceutical industries, Rev. Agric. Sci. 4 (2016) 56–65, https://doi.org/10.7831/ras.4.56.
[59] E.E. Ekanem, Z. Zhang, G.T. Vladisavljević, Facile microfluidic production of composite polymer core-shell microcapsules and crescent-shaped microparticles, J. Colloid Interface Sci. 498 (2017) 387–394, https://doi.org/10.1016/j.jcis.2017.03.067.
[60] S.A. Nabavi, G.T. Vladisavljević, V. Manović, Mechanisms and control of single-step microfluidic generation of multi-core double emulsion droplets, Chem. Eng. J. 322 (2017) 140–148, https://doi.org/10.1016/j.cej.2017.04.008.
[61] R. Santiago, J. Lemus, C. Moya, D. Moreno, N. Alonso-Morales, J. Palomar, Encapsulated ionic liquids to enable the practical application of amino acid-based ionic liquids in CO2 capture, ACS Sustain. Chem. Eng. 6 (2018) 14178–14187, https://doi.org/10.1021/acssuschemeng.8b02797.
[62] M. Nisar, F.L. Bernard, E. Duarte, V.V. Chaban, S. Einloft, New polysulfone microcapsules containing metal oxides and ([BMIM][NTf2]) ionic liquid for CO2 capture, J. Environ. Chem. Eng. 9 (2021), https://doi.org/10.1016/j.jece.2020.104781.
[63] J.K. Stolaroff, C. Ye, D.T. Nguyen, J. Oakdale, J.M. Knipe, S.E. Baker, CO2 absorption kinetics of micro-encapsulated ionic liquids, Energy Proc. 114 (2017) 860–865, https://doi.org/10.1016/j.egypro.2017.03.1228.
[64] E.D. Isaacs-Páez, A.J. García-Pérez, C. Nieto-Delgado, L.F. Chazaro-Ruiz, J. R. Rangel-Mendez, Enhanced CO2 capture kinetics by using macroporous carbonized natural fibers impregnated with an ionic liquid, J. Mol. Liq. 350 (2022), 118602, https://doi.org/10.1016/j.molliq.2022.118602.
[65] R. Santiago, J. Lemus, D. Moreno, C. Moya, M. Larriba, N. Alonso-Morales, M. A. Gilarranz, J.J. Rodríguez, J. Palomar, From kinetics to equilibrium control in CO2 capture columns using encapsulated ionic liquids (ENILs), Chem. Eng. J. 348 (2018) 661–668, https://doi.org/10.1016/j.cej.2018.05.029.